CHEMISTRY

A photovoltaic-electrolysis system with high solar-to-hydrogen efficiency under practical current densities

Qingran Zhang[1,2]†, Yihao Shan[1]†, Jian Pan[1,3], Priyank Kumar[1], Mark J. Keevers[4], John Lasich[5], Gurpreet Kour[1], Rahman Daiyan[1], Ivan Perez-Wurf[4], Lars Thomsen[6], Soshan Cheong[7], Junjie Jiang[1], Kuang-Hsu Wu[1], Chao-Lung Chiang[8], Kristian Grayson[5], Martin A. Green[4], Rose Amal[1]*, Xunyu Lu[1]*

The photovoltaic-alkaline water (PV-AW) electrolysis system offers an appealing approach for large-scale green hydrogen generation. However, current PV-AW systems suffer from low solar-to-hydrogen (STH) conversion efficiencies (e.g., <20%) at practical current densities (e.g., >100 mA cm^{-2}), rendering the produced H_2 not economical. Here, we designed and developed a highly efficient PV-AW system that mainly consists of a customized, state-of-the-art AW electrolyzer and concentrator photovoltaic (CPV) receiver. The highly efficient anodic oxygen evolving catalyst, consisting of an iron oxide/nickel (oxy)hydroxide (Fe_2O_3-NiO_xH_y) composite, enables the customized AW electrolyzer with unprecedented catalytic performance (e.g., 1 A cm^{-2} at 1.8 V and 0.37 kgH_2/m^{-2} $hour^{-1}$ at 48 kWh/kgH_2). Benefiting from the superior water electrolysis performance, the integrated CPV-AW electrolyzer system reaches a very high STH efficiency of up to 29.1% (refer to 30.3% if the lead resistance losses are excluded) at large current densities, surpassing all previously reported PV-electrolysis systems.

INTRODUCTION

Hydrogen (H_2) is a promising energy carrier that can effectively store renewable electricity (e.g., generated by photovoltaics or wind turbines) in the form of chemical energy, thereby bypassing the intermittency issue of renewable resources and fulfilling their continuous usage purpose. Besides, in global markets, H_2 can also be traded as a clean energy commodity, which satisfies the intercontinental carbon neutralization agreement between those major and rising economies. Therefore, the development of clean and efficient H_2 production technologies is highly sought after. Currently, among various H_2 generation approaches, photovoltaic (PV) powered water electrolysis (WE) represents the most mature technology for green hydrogen production as both PV and WE components are commercially manufactured at large scale. Moreover, the versatile nature of both PV and WE technology also enables the green H_2 generation at different scales in a decentralized manner, thus necessitating the attainment of advanced PV-WE systems per demand. Recently, because of considerable breakthroughs in material science and cell manufacturing, the past few decades have witnessed a rapid technological advancement in the PV industry, with the solar-to-electricity efficiency reaching a record of 47.1% in 2023 (*1*). However, the overall solar-to-hydrogen (STH) conversion efficiency during the PV-WE process is still severely constrained by the sluggish WE kinetics, which leads to huge energy consumption and cost for H_2 production. In this regard, the development of efficient WE technologies that can achieve both high energy efficiency and low cost is highly desired. Typically, the industrially practiced low-temperature WE technologies can be mainly divided into two categories, namely, alkaline water (AW) electrolysis and proton-exchange membrane (PEM) electrolysis. PEM electrolyzers normally exhibit higher energy efficiency and power density than AW electrolyzers (AWEs), while the necessity of using precious metals, both as the catalyst materials and the current collector coatings, has rendered their global scale deployment unsustainable. In contrast, the AWE, as the most mature WE technology, has been commercialized for more than a century and is currently manufactured at gigawatt scale with a much lower capital expenditure [€750 ($773.45 USD) per kilowatt] than that of PEM counterparts [€1200 ($1237.52 USD) per kilowatt] (*2*). Nevertheless, compared with PEM devices, the AW electrolysis is still largely limited by the low energy efficiency at high current densities (e.g., less than 70% at current densities over 0.3 A cm^{-2}), thereby stagnating the further reduction of green H_2 cost. Notably, in alkaline electrolytes, despite the development of anion exchange membrane (AEM) technologies showing promises in achieving a high WE efficiency, the stability of those AEM setups still calls for further improvement to meet the durability requirements for their large-scale applications. Under the ideal scenario, if the performance of AWEs can be improved drastically to reach a level that approaches PEM technology (e.g., reaching a current density of 0.3 and 1 A cm^{-2} at applied voltages of no higher than 1.6 and 1.8 V, respectively), the capital cost of green H_2 can be decreased substantially, benefiting a sustainable H_2 economy. To this end, tremendous research effort has been made to improving the overall AW electrolysis efficiency,

[1]Particles and Catalysis Research Group, School of Chemical Engineering, The University of New South Wales, Sydney, NSW 2052, Australia. [2]State Key Laboratory of Pollution Control and Resources Reuse, School of Environmental Science and Engineering, Tongji University, 1239 Siping Road, Shanghai 200092, China. [3]Shanghai WarpEnergy Co. Ltd., Building 24, 1818 Chengbei Road, Shanghai 201807, China. [4]School of Photovoltaic and Renewable Energy Engineering, University of New South Wales, Sydney, NSW 2052, Australia. [5]RayGen Resources Pty. Ltd., 8 Cato Street, Hawthorn East, Victoria 3123, Australia. [6]Australian Synchrotron, Australian Nuclear Science and Technology Organization, 800 Blackburn Road, Clayton, Victoria 3168, Australia. [7]Electron Microscope Unit, Mark Wainwright Analytical Centre, The University of New South Wales, Sydney, NSW 2052, Australia. [8]Material Science Group, Scientific Research Division, National Synchrotron Radiation Research Center, Hsinchu 30076, Taiwan.
*Corresponding author. Email: r.amal@unsw.edu.au (R.A.); xunyu.lu@unsw.edu.au (X.L.)
†These authors contributed equally to this work.

including but not limiting to electrolyzer engineering, cell performance modeling, and the design of efficient electrocatalysts (*3*–*6*).

Among many attempts aimed to mitigate the AWE energy losses, designing the efficient oxygen evolving electrocatalysts plays a pivotal role in enabling a high-rate electrolysis process. This is mainly attributed to the huge energy barriers associated with the four proton-coupled electron transfer steps of the anodic oxygen evolution reaction (OER), where a scaling relationship among oxygen intermediates has long stagnated the improvement of its kinetics (*7*). Hence, material innovation/breakthroughs are indeed needed to attain high-performance catalysts to overcome the sluggish reaction kinetics of OER. Fortunately, the past few decades have witnessed a surge in the development of oxygen evolving catalysts, especially those first-row transition metal–based (TM) materials. Because of their tunable electronic properties, the TM electrocatalysts exhibit great promise in delivering high intrinsic OER activities at low overpotential range, including but not limited to the geled FeCoW (*8*) oxyhydroxides, exfoliated NiFe-layered double hydroxide (*9*), Co-Zn oxyhydroxide (*10*), and mass-selected Ni(Fe)O_xH_y nanoparticles (NPs) (*11*). However, despite some progress, the inherent OER activity of these materials is still unsatisfactory, which is severely constrained by the scaling relationship between each reactive intermediate and the slow charge/spin transport within such catalytic processes (*12*, *13*). This insufficiency not only limits their ability to effectively mitigate the sluggish OER kinetics, but also results in poor current densities at low applied overpotentials. Further, when an enlarged surface area is applied to the electrocatalysts (such as from ~1 cm^2 to over 100 cm^2), the apparent catalytic performance of the OER electrodes developed tends to decline quickly. This inevitably poses a great challenge when attempting to scale up these state-of-the-art OER electrodes, which largely stagnates their practical applications in the WE industry. Therefore, it is of paramount importance to design the efficient OER catalysts/electrodes with a high intrinsic activity that can be effectively retained when scaled up, providing opportunities to improve the AW electrolysis performance that can benefit a high STH efficiency with cost-effectiveness.

Here, we present a practical PV-WE system that can maintain a high STH efficiency at large current density. By developing a multicomponent OER catalyst with exceptional performance, a high-rate AW electrolyzer is designed and fabricated, which is distinctive for its high energy efficiency at large current densities. This matches well with the state-of-the-art high-performance CPV receiver that in turn benefits an efficient STH conversion. Notably, the efficient OER catalyst developed in this work is mainly composed of ultrasmall Fe_2O_3 NPs loaded on nickel (oxy)hydroxide (Fe_2O_3-NiO_xH_y) nanosheets. Because of the ultrasmall nature of iron oxide, abundant catalytic interfaces can be formed between Fe_2O_3 and NiO_xH_y species, providing two different neighboring adsorption sites for expediting the OER process. Through theoretical computations and spectroscopic experiments, it was indicated that the OER can proceed through a bifunctional mechanism on such composites, where two kinds of different adsorption sites facilitate the independent tailoring of binding strength for each intermediate, thereby enabling an accelerated OER kinetics. As a result, the oxygen electrodes based on the Fe_2O_3-NiO_xH_y composite exhibit exceptionally high OER activity in 1 M KOH, reaching a current density of 100 and 500 mA cm^{-2} with less than 230 and 400 mV of overpotentials, respectively, in the absence of any *iR* corrections. In addition, using the Fe_2O_3-NiO_xH_y–based oxygen electrode as the anode, a high-performance AWE is fabricated, which delivers large current densities of 0.5 A cm^{-2} and 1 A cm^{-2} at applied cell voltages of merely 1.65 and 1.80 V (no *iR* corrections, in hot KOH solution), respectively. Further integrating such high-rate AWE with a state-of-the-art concentrator PV (CPV) receiver yields a high-performance CPV-AW system, which demonstrates a record-breaking STH efficiency of 29.1% (correspond to 30.3% excluding the lead resistance losses) under large current densities (up to 240 mA cm^{-2}), providing valuable knowledge for designing electrolysis systems (including catalysts and PV-WE devices) that can generate green hydrogen efficiently from solar energy.

RESULTS

Synthesis and characterization

The Fe_2O_3-NiO_xH_y composite in this work is first prepared on the surface of nickel foam (NF) substrate through a controllable hydrothermal process in weak alkaline environment (see details in Materials and Methods). In brief, a solution of methanol and water, containing iron nitrate and ethylenediaminetetraacetic acid anions ($EDTA^{4-}$), was introduced into a Teflon-lined autoclave in the presence of NF. During the hydrothermal reaction, the Ni species in NF react with the hydroxide ions, forming ultrathin nickel oxyhydroxide (NiO_xH_y) nanosheets (see details in fig. S1). Then, the slow release of metal cations from Fe-EDTA complexes in methanol solution enabled a controllable hydrolysis rate of Fe^{3+}, which eventually results in the formation of numerous ultrasmall Fe_2O_3 NPs on the surface of NiO_xH_y nanosheets. Scanning electron microscopy (SEM) analysis revealed that the hydrothermal process has resulted in the formation of a highly rippled and interconnected nanosheet structure on the surface of the NF skeleton (Fig. 1A and fig. S2). This is in stark contrast to the morphology of the NF before the reaction (fig. S2). Transmission electron microscopy (TEM) images (Fig. 1B and fig. S3) showed that the electrocatalyst produced through the as-prepared method is composed of a thin nanosheet structure decorated with numerous ultrafine NPs (between 5 and 10 nm), which is further echoed by the atomic-resolution scanning TEM in high-angle annular dark-field mode (HAADF-STEM; Fig. 1D and fig. S4). The clear lattice fringes of approximately 0.27 nm on the NPs (Fig. 1C) provide additional evidence for the highly crystalline structure of the NPs. These fringes can be assigned to the ⟨104⟩ planes of a hematite structure, which is confirmed by the fast Fourier transform pattern derived from the image in Fig. 1C. Upon further analysis of the HAADF-STEM image and the corresponding energy-dispersive x-ray spectroscopy (EDS) maps (Fig. 1, D to G, and fig. S4) from a selected area of Fe_2O_3-NiO_xH_y, it was observed that there is a spatially separated distribution of Ni and Fe elements across the composite. The Fe signals were primarily concentrated on the NPs, while the Ni element was detected throughout the entire nanosheet structure. Notably, the electron energy-loss spectroscopy (EELS) measurements (fig. S5) have further provided evidence of the absence of Fe signals in the nanosheet area, suggesting that the nanosheet is predominantly composed of NiO_xH_y, rather than $NiFeO_xH_y$. Furthermore, through the atomic force microscopy characterization (fig. S6), an average thickness of 1 nm was revealed for the iron oxide NPs, which confirms a characteristic feature of the planar hematite structure that may include a four-layer stacking of O-Fe-Fe-O units (*9*). Hence, the above results all indicate that the as-synthesized catalysts are mainly composed of

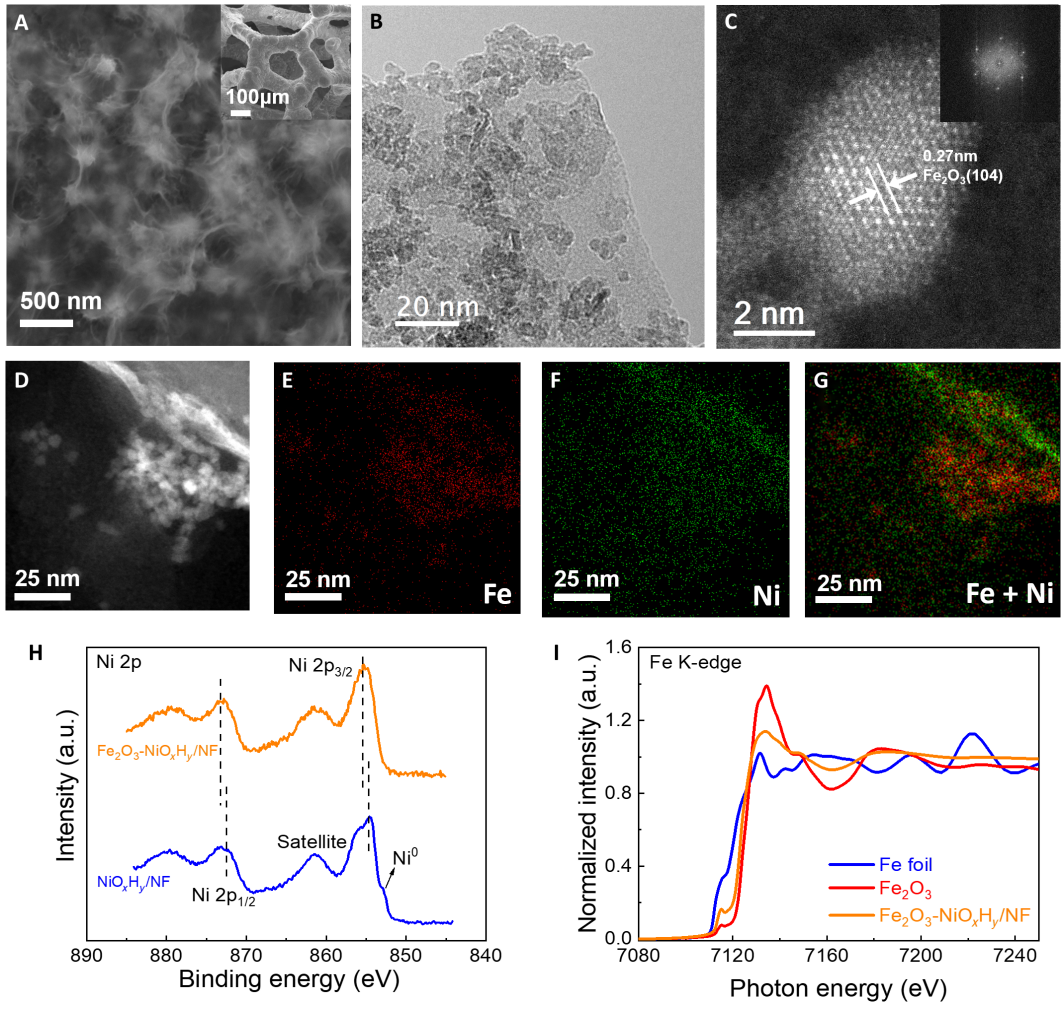

Fig. 1. Microstructural analysis of the Fe_2O_3-NiO_xH_y catalyst. (**A**) SEM images of Fe_2O_3-NiO_xH_y/NF electrode under different magnifications. (**B**) TEM image of Fe_2O_3-NiO_xH_y showing a nanosheet structure loaded with abundant NPs. (**C**) HAADF-STEM image of the ultrafine Fe_2O_3 NPs showing a hexagonal structure. Inset is the fast Fourier transform pattern of ultrafine Fe_2O_3 NPs. (**D**) HAADF-STEM image of the Fe_2O_3-NiO_xH_y catalyst and the corresponding EDS elemental maps of (**E**) Fe and (**F**) Ni derived from Fe_2O_3-NiO_xH_y composite in (D). (**G**) Overlapped elemental maps of Fe and Ni derived from Fe_2O_3-NiO_xH_y composite in (D). (**H**) Ni 2p XPS spectra of Fe_2O_3-NiO_xH_y/NF and NiO_xH_y/NF electrode. (**I**) Fe K-edge XANES spectra of ultrasmall Fe_2O_3 NPs, bulk Fe_2O_3 NPs, and Fe foil.

Ni (oxy)hydroxide nanosheets decorated with numerous ultra-small Fe_2O_3 NPs.

To gain a deeper understanding of the interactions between the Fe_2O_3 and NiO_xH_y components in the composite, x-ray photoelectron spectroscopy (XPS) measurements were conducted. It was revealed that the formation of ultrasmall Fe_2O_3 NPs on the NiO_xH_y nanosheet does not disturb the valence state of Ni species, exhibiting the similar Ni 2p spectra on both NiO_xH_y/NF and Fe_2O_3-NiO_xH_y/NF that are dominated by Ni^{2+} (Fig. 1H), in conformity with the Ni L-edge EELS measurements (fig. S5). However, compared to the pure NiO_xH_y nanosheets, the Ni $2p_{3/2}$ peak of Fe_2O_3-NiO_xH_y/NF shifts positively to the higher binding energy side, indicating a strong electronic interaction between NiO_xH_y and Fe_2O_3 species after forming the hybrid Fe_2O_3-NiO_xH_y catalysts. This phenomenon can be further confirmed by the Fe 3p measurements (fig. S7), showing a negative shift of the Fe 3p spectrum on Fe_2O_3-NiO_xH_y/NF, which illustrates a possible electron transfer from the NiO_xH_y to the Fe_2O_3 NPs. To further investigate the chemical state of Fe species that possibly correlates to such interaction within Fe_2O_3-NiO_xH_y, x-ray absorption spectroscopy (XAS) characterizations were performed. As shown in Fig. 1I, the Fe K-edge x-ray absorption near-edge spectra (XANES) features a main absorption edge at ≈7133.8 eV, which is due to the dipole-allowed 1s → 4p orbital transition. Notably, after forming the hybrid Fe_2O_3-NiO_xH_y catalysts, the main absorption peak intensity is decreased (fig. S8), implying a reduced Fe 4p unoccupied state that might be originated from the gain of charges at Fe atoms in Fe_2O_3-NiO_xH_y in comparison with pure ultrasmall Fe_2O_3 NPs. This further supports the observations in XPS that the electronic interactions between Fe_2O_3 and NiO_xH_y species would lead to an interfacial charge transfer that might be beneficial for OER catalysis. Moreover, compared to the bulk Fe_2O_3 NPs (see preparation method in Materials and Methods), the Fe_2O_3-NiO_xH_y exhibits way higher pre-edge intensity and a decrease in white line intensity, together with a shift of main absorption edge to low energy side (~0.4 eV). This not only indicates a lower local oxygen coordination of Fe atoms but also further evidences an electron-rich Fe_2O_3 phase in Fe_2O_3-NiO_xH_y catalysts

(*14*). Through the corresponding Fourier-transformed extended x-ray absorption fine structure (XAFS) Fe K-edge spectra (fig. S9), an average coordination number of 3.4 and 5.8 was revealed for Fe_2O_3-NiO_xH_y and bulk Fe_2O_3 NPs (table S1), respectively, suggesting a defective nature of ultrasmall Fe_2O_3 NPs in the Fe_2O_3-NiO_xH_y catalysts. This is also confirmed by XPS O 1s spectra (fig. S10) that more O vacancies exist in Fe_2O_3 of Fe_2O_3-NiO_xH_y and might be beneficial for the OER process (*15*, *16*). Therefore, on the basis of the x-ray spectroscopic characterizations above, it was evident that the formation of Fe_2O_3-NiO_xH_y has resulted in an electronic interaction between Fe_2O_3 and NiO_xH_y species that in turn generates an electron-rich Fe_2O_3 phase with O defects.

Electrocatalytic OER performance

The electrochemical OER performances of the electrodes prepared were first evaluated in a purified 1 M KOH solution at a scan rate of 1 mV s^{-1}. As shown in Fig. 2A, Fe_2O_3-NiO_xH_y/NF exhibits the earliest onset potential [~1.42 V versus reversible hydrogen electrode (RHE)] among the three electrodes tested, and only requires an overpotential of 290 mV to reach a current density (*j*) of 100 mA cm^{-2} without any *iR* correction (see *iR*-corrected results in fig. S11). The presence of the Fe_2O_3-NiO_xH_y composite is apparently more advantageous in catalyzing the OER, as the NiO_xH_y/NF and pure NF electrodes call for additional 130 and 220 mV of overpotential to reach the same *j* of 100 mA cm^{-2}. The enhanced activity on Fe_2O_3-NiO_xH_y could be

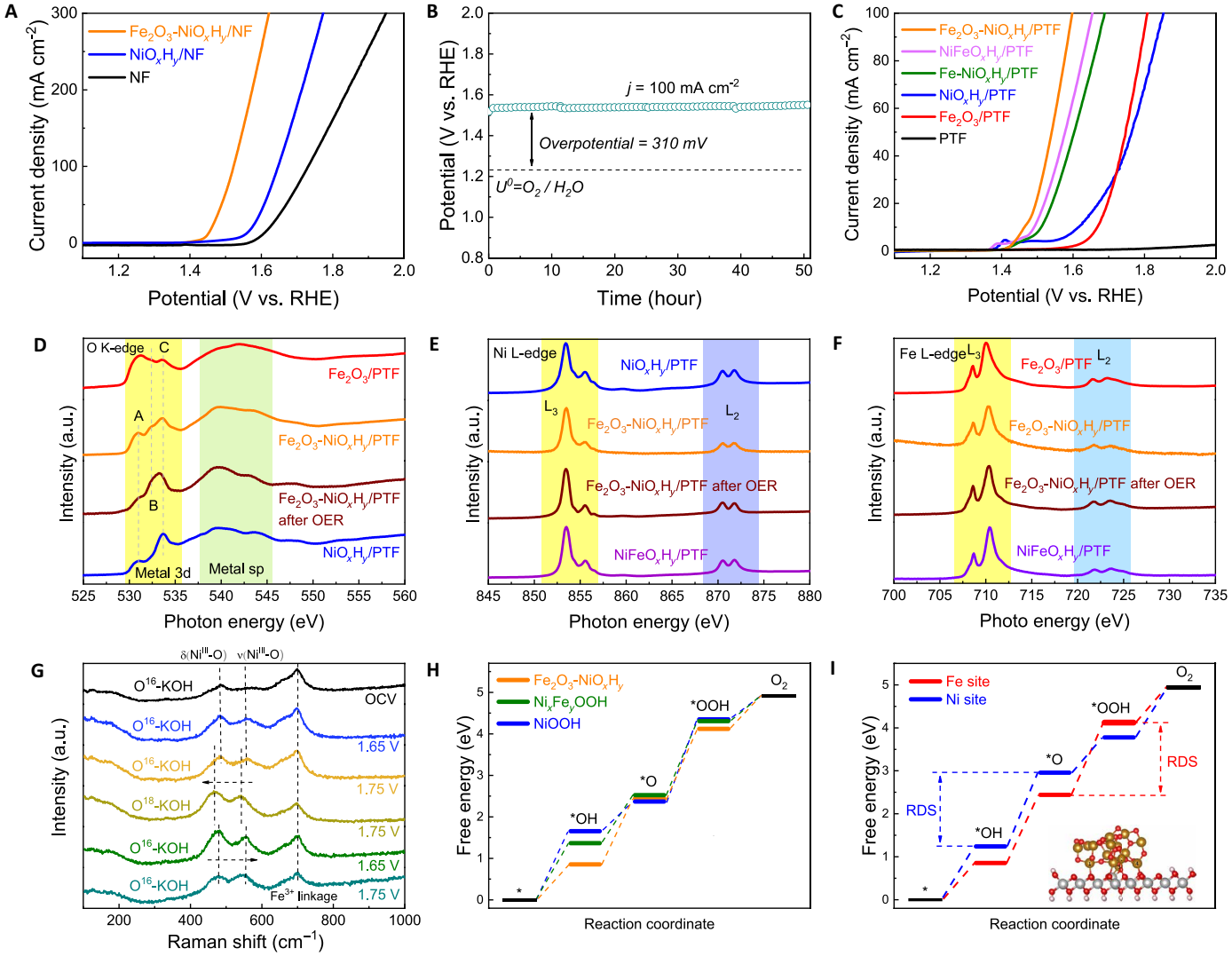

Fig. 2. Electrochemical measurements of Fe_2O_3-NiO_xH_y/NF, Fe_2O_3-NiO_xH_y/PTF, and relevant mechanism studies in purified 1 M KOH. (**A**) OER polarization curves of Fe_2O_3-NiO_xH_y/NF, NiO_xH_y/NF, and pure NF with a scan rate of 1 mV s^{-1} (no *iR* correction). (**B**) The long-term durability test on Fe_2O_3-NiO_xH_y/NF evaluated at 100 mA cm^{-2}. (**C**) OER polarization curves of Fe_2O_3-NiO_xH_y/PTF, $NiFeO_xH_y$/PTF, Fe-NiO_xH_y/PTF, NiO_xH_y/PTF, Fe_2O_3/PTF, and pure PTF electrodes in purified 1 M KOH without *iR* correction. (**D**) O K-edge soft x-ray absorption spectroscopy (sXAS) spectra of Fe_2O_3-NiO_xH_y/PTF, postreaction Fe_2O_3-NiO_xH_y/PTF, NiO_xH_y/PTF, and Fe_2O_3/PTF. The O K-edge peaks in yellow area are correlated to the transitions to unoccupied oxygen 2p states hybridized with the metal 3d band, while the green area represents oxygen 2p character hybridized with metal 4s and 4p states. (**E**) Ni and (**F**) Fe L-edge sXAS spectra of Fe_2O_3-NiO_xH_y/PTF, postreaction Fe_2O_3-NiO_xH_y/PTF, $NiFeO_xH_y$/PTF, Fe-NiO_xH_y/PTF, and Fe_2O_3/PTF. (**G**) In situ Raman spectra of Fe_2O_3-NiO_xH_y/PTF obtained at various potentials for oxygen isotope labeling in 0.1 M KOH-$H_2{}^{18}O$ solution and subsequent isotope exchange experiments. (**H**) The free-energy diagram of the OER processes on Fe_2O_3-NiO_xH_y, NiFeOOH, and NiOOH. (**I**) The free-energy diagram of the OER processes on Fe (fig. S22) and Ni site (fig. S28) of Fe_2O_3-NiO_xH_y catalysts. The inset shows the structure model of Fe_2O_3-NiO_xH_y catalysts used for DFT simulations.

mainly attributed to the formation of numerous boundary sites between the Fe_2O_3 and NiO_xH_y components, which is beneficial to lower the energy barriers of OER process, as evidenced by a lower catalytic performance on samples with less Fe_2O_3-NiO_xH_y interfaces (figs. S12 and S13). Considering the ubiquitous appearance of iron impurities in the environment, the possible origin of OER activity from a NiFeOOH composite cannot be fully excluded. Thus, electrodeposited NiFe oxyhydroxide and Fe-incorporated Fe_2O_3-NiO_xH_y electrocatalysts on an NF skeleton (named as $NiFeO_xH_y$/NF and Fe_2O_3-$NiFeO_xH_y$/NF, respectively; see preparation details in Materials and Methods) were further prepared and evaluated under the identical testing conditions. It was indicated in fig. S14 that the OER activities on $NiFeO_xH_y$/NF and Fe_2O_3-$NiFeO_xH_y$/NF were much lower than that of Fe_2O_3-NiO_xH_y/NF in terms of both onset potential (E_{onset}) and current density (j), suggesting that the high OER performance on Fe_2O_3-NiO_xH_y/NF electrode is originated from neither the NiFeOOH species nor the incorporated Fe impurities. To meet the requirements of practical PV-WE devices, the long-term stability on Fe_2O_3-NiO_xH_y/NF was also evaluated at 100 mA cm^{-2}. As can be seen from Fig. 2B, no obvious decay of OER activity can be observed on Fe_2O_3-NiO_xH_y/NF after over 50 hours durability test, demonstrating a good stability of the Fe_2O_3-NiO_xH_y catalyst. The same conclusion can be further supported by the accelerated durability tests, which exhibits no decay of catalytic behavior after 5000 cyclic voltammetry scans (fig. S15).

The above results have clearly indicated the advantageous role of the Fe_2O_3-NiO_xH_y composite in advocating OER, while the spurious effects arising from the interaction between the composite and NF need to be precluded to explore its intrinsic activity. In this case, platinized titanium fiber (PTF) is used as a highly conductive and nonreactive substrate. Apart from Fe_2O_3-NiO_xH_y, Fe_2O_3 NPs, and NiO_xH_y, the OER benchmarks, including the electrodeposited NiFe oxyhydroxide ($NiFeO_xH_y$) and Fe-incorporated NiO_xH_y (Fe-NiO_xH_y), are also prepared on PTF as the control samples (see details in Materials and Methods). As expected, Fe_2O_3-NiO_xH_y/PTF (figs. S16 and S17) exhibits the best OER activity in the rigorously purified 1 M KOH among all samples (Fig. 2C), further verifying the highly active nature of the Fe_2O_3-NiO_xH_y composite. The exceptional OER performance of Fe_2O_3-NiO_xH_y/PTF can be also reflected by its lowest Tafel slope (46 mV per decade; fig. S18) among all the samples tested here, suggesting the important role of the interplay between Fe_2O_3 and NiO_xH_y in promoting the OER. Furthermore, the possible enhancement effect of Fe impurities on the OER behavior of Fe_2O_3-NiO_xH_y was also excluded by Fe-spiking experiments, showing a slightly decreased OER performance after Fe spiking (fig. S19), which indicates that the superior catalytic activity on Fe_2O_3-NiO_xH_y is not correlated to the Fe-incorporation phenomenon during OER. To further evaluate the intrinsic OER activity of Fe_2O_3-NiO_xH_y, we calculated the turnover frequencies on the PTF-based electrodes [turnover frequencies (TOFs); table S2, details can be found in the Supplementary Materials]. The Fe_2O_3-NiO_xH_y exhibits TOFs of 0.86 s^{-1} per Fe atoms, which is not only at least a magnitude higher than the other PTF electrodes but also way higher than most of the advanced OER catalysts reported so far (table S2). Considering the fact that the amount of Fe atoms used in TOF calculation is much higher than that of edge sites in Fe_2O_3 within the active Fe_2O_3-NiO_xH_y interface, the intrinsic OER activity of Fe_2O_3-NiO_xH_y/PTF is clearly underestimated herein.

Spectroscopic analysis and mechanistic investigation

Through soft XAS (sXAS), the chemical state of Ni and Fe atoms within Fe_2O_3-NiO_xH_y active species was further investigated carefully using the PTF-based electrodes to exclude the possible influence from metallic substrate (such as Ni foam). As can be seen from Fig. 2E, after forming the Fe_2O_3-NiO_xH_y hybrid catalysts, the Ni L-edge near-edge XAFS (NEXAFS) spectroscopy of Fe_2O_3-NiO_xH_y/PTF shifted positively to the higher energy side compared with that of NiO_xH_y/PTF, evidencing an electronic interaction between Fe_2O_3 and NiO_xH_y species that induces possible charge transfer from Ni to Fe atoms, as supported by XPS measurements. In addition, further postreaction sXAS measurements were also performed to investigate the OER process within Fe_2O_3-NiO_xH_y catalysts. It was indicated that no obvious changes have been detected in the Ni and Fe L-edge NEXAFS spectroscopy of Fe_2O_3-NiO_xH_y/PTF before and after OER measurements (Fig. 2, E and F), revealing a dominant Ni^{2+} and Fe^{3+} state in the catalysts. In contrast, after OER, the O K-edge NEXAFS spectra of Fe_2O_3-NiO_xH_y/PTF exhibit obvious variations in those pre-edge features (529 to 535 eV; Fig. 2D), which correspond to the transitions to unoccupied oxygen 2p states that are hybridized with the metal 3d band (*17*, *18*). Notably, in the O K-edge spectra of the Fe_2O_3-NiO_xH_y/PTF electrode, two pre-edge features can be observed, which represent the metal 3d e_g-t_{2g} symmetry that are separated by oxygen octahedral (O_h) crystal field (ligand-field splitting) (*18*, *19*). After OER, these pre-edge intensity of Fe_2O_3-NiO_xH_y/PTF decreases slightly, suggesting the possible variation of oxygen content in Fe_2O_3-NiO_xH_y during the O_2-evolving reaction (*20*), which might lead to O vacancies or lattice O replacement in the catalysts (*21*). Furthermore, it is worth noting that the splitting of such pre-edge peak becomes less obvious after the OER process, showing the merge of t_{2g} and e_g features. This can be correlated to an increased degree of multiplicity on Fe or Ni sites (*19*), as the OER process involving a possible lattice O replacement mechanism may create structure disorder in the catalysts.

Further in-depth study of the OER process on Fe_2O_3-NiO_xH_y was carried out through in situ Raman measurements. It was revealed that the NiO_xH_y species within Fe_2O_3-NiO_xH_y catalysts deprotonates [e.g., α-$Ni(OH)_2$ → γ-NiOOH] gradually along with an applied anodic potential (fig. S20), showing an increased intensity of two apparent peaks at 480 and 560 cm^{-1} that corresponds to the e_g bending [$\delta(Ni^{III}\text{-}O)$] and the A_{1g} stretching [$\upsilon(Ni^{III}\text{-}O)$] vibration of Ni-O in γ-NiOOH, respectively (*22*). In contrast, the A_{1g} mode (700 cm^{-1}) featured in a Fe_2O_3 structure exhibits negligible changes upon an applied anodic bias (*23*, *24*), indicative of an electrochemically inert property of Fe_2O_3 that remains a stable crystal structure during OER. The higher relative intensities of the 480 and 560 cm^{-1} bands (I_B/I_S) in Fe_2O_3/NiO_xH_y under the anodic potentials might be ascribed to the formation of disordered Ni oxyhydroxide structure at high overpotential range, in consistency with the previous reports (*22*, *25*). Notably, no obvious $NiOO^-$ signal (active oxygen, ~1000 cm^{-1}) is observed on Fe_2O_3-NiO_xH_y under all OER conditions, suggesting that the $NiOO^-$ is not the precursor for dioxygen. Previous reports depicted that the redox of Ni species during OER process may lead to the participation of lattice oxygen in the catalytic cycle (*26*, *27*). Thus, to verify the possible role of lattice oxygen, isotope labeling experiments were also performed. During the experiments, the Fe_2O_3-NiO_xH_y/PTF electrode was first activated in 0.1 M ^{18}O-KOH solution and then subjected to positive potential in electrolyte with $H_2{}^{16}O$. As can be seen from Fig. 2G, after the activation process, the $\delta(Ni^{III}\text{-}O)$

and υ(Ni^{III}-O) Raman peaks of Fe_2O_3-NiO_xH_y/PTF both shifted negatively by 15 cm^{-1} to lower frequencies (Fig. 2G), which is mainly due to the effect of O mass on vibration modes, suggesting the successful ^{18}O labeling of lattice oxygen. Then, the ^{18}O-labeled Fe_2O_3-NiO_xH_y catalysts were placed immediately back to 0.1 M ^{16}O-KOH under an OER potential. After this process, it is worth noting that the δ(Ni^{III}-O) and υ(Ni^{III}-O) features both shifted positively back to higher frequencies, indicative of the partial exchange of lattice oxygen on Fe_2O_3-NiO_xH_y composites, which echoes well with the NEXAFS O K-edge results (*25*). Within a Ni-(oxy)hydroxide–based multicomponent catalyst, the exchange of lattice O normally suggests the emergence of Ni^{2+} during a catalytically active Ni(II/III) redox cycle, where a possible bifunctional mechanism could proceed that enables the regeneration of Ni^{II}-O species (*25*). In contrast, for those Fe-incorporated NiOOH that follows a single reactive site mechanism, previous reports suggest no observation of lattice O exchange in the catalysts (*26*, *28*). To this end, it is plausible to postulate that two kinds of catalytic adsorption sites (such as Ni in NiO_xH_y and Fe in Fe_2O_3) might be actively involved in the OER process of Fe_2O_3-NiO_xH_y catalysts. As a result, the adsorption state of those key OER intermediates could be tailored independently on two different active species, thereby bypassing the scaling relationship for enhanced reaction kinetics. Thus, collectively, on the basis of the above spectroscopic experiments, it is evident that the lattice oxygen might participate in OER of Fe_2O_3-NiO_xH_y catalysts, which may lead to a bifunctional mechanism where NiO_xH_y and Fe_2O_3 species act synergistically to accelerate OER kinetics.

To further elucidate the as-proposed OER mechanism, density functional theory (DFT) simulations were conducted. Previous theoretical and experimental investigations suggested that γ-NiOOH is more likely to form under the anodic OER potentials (*29*, *30*), while α-Fe_2O_3 remains stable within most electrocatalytic processes. Moreover, in this work, combined microscopic measurements identified the coexistence of α-Fe_2O_3 and γ-NiOOH species even after the durability tests (fig. S21), where the former located uniformly on top of the latter composites. Therefore, during the computational studies, a model with α-Fe_2O_3 cluster attached on top of a γ-NiOOH monolayer was adopted to represent our catalyst structure (Fig. 2I). On the basis of previous reports, the four-step OER mechanism proposed by Rossmeisl *et al.* (*31*) was used for the theoretical simulations. For comparison, numerous potential active sites within such catalyst structure were screened (fig. S22), and the catalytic behavior of pure α-Fe_2O_3, γ-NiOOH, and benchmark Fe-doped Ni oxyhydroxide ($NiFeO_xH_y$) composites was also simulated to verify the genuine active species. As shown in Fig. 2H and figs. S23 and S24, we find that the Fe edge sites of α-Fe_2O_3, which bond covalently with the γ-NiOOH substrate, exhibit a superior OER behavior and the lowest overpotential than the other active moieties, which even surpasses the benchmark Fe sites in a doped Ni oxyhydroxide (fig. S25 and Fig. 2H), giving an overpotential value of only 0.45 V (fig. S26). In contrast, the pure α-Fe_2O_3 and γ-NiOOH (Fig. 2H and fig. S27) both have high overpotential values for OER (fig. S26), in consistency with the previous reports (*32*, *33*). Furthermore, the Fe edge sites that bridge the α-Fe_2O_3 NP and γ-NiOOH substrate provide opportunities to facilitate OER through a multisite functionality (*34*, *35*), where different active atoms can act synergistically to stabilize one transition state (such as OOH*) without stabilizing the others (e.g., OH*), bypassing the scaling relationship that far limits OER kinetics. In this regard, the Gibbs free energies of both Fe and Ni atoms at the α-Fe_2O_3-γ-NiOOH interface were investigated. It is revealed that the formation of OOH* intermediate is the rate-determining step (RDS) on the Fe edge site of α-Fe_2O_3 (fig. S22), while the RDS on Ni site sited at the α-Fe_2O_3-γ-NiOOH interface (fig. S28 and 29) is the formation of OH* species (Fig. 2I). To this end, if the Fe and Ni atoms located at the α-Fe_2O_3-γ-NiOOH interface act synergistically to form the OH* and OOH*, respectively, the OER overpotential can be further decreased due to the breaking of scaling relationship for OER. Thus, theoretical modeling above indicates a superior OER performance on the Fe_2O_3-NiO_xH_y catalysts, which is mainly due to the optimized adsorption energy on the Fe_2O_3 edge sites. Further multisite simulations suggest a possible bifunctional mechanism where Fe atoms on the edge of ultrasmall α-Fe_2O_3 clusters can act synergistically with Ni atoms in oxyhydroxide to facilitate the formation of necessitate OER intermediates, providing opportunities to bypass the scaling relationship limit.

Scaled fabrication of Fe_2O_3-NiO_xH_y/FeF electrode

Notably, although the above electrochemical measurements based on Ni foam and PTF substrates all confirmed a superior OER activity and stability on the Fe_2O_3-NiO_xH_y composites, it remains a grand challenge to further scale up the laboratory-based active electrodes in terms of size and catalyst loading to afford an improved apparent activity, especially on an enlarged geometric surface area, thus far impairing those laboratory-derived active electrocatalysts from the industrial electrolysis. Here, because of the limited amount of NiO_xH_y species generated on the NF skeleton during the hydrothermal process (fig. S1), further increasing the loading of Fe_2O_3 NPs will not lead to the formation of more active interfaces between iron oxide and nickel oxyhydroxide, resulting in a decreased current density alongside with the enlarged electrode size. To resolve this issue, we electrodeposited ample amount of Ni oxyhydroxide on the iron foam (FeF) skeleton to create more Fe_2O_3-NiO_xH_y active interfaces for an improved apparent OER performance (see details in Materials and Methods), which helps to satisfy the WE requirements (ampere level) in a practical PV-WE device, where large current densities at low overpotentials are indeed needed to match up with the PV performance. Through combined microscopic and spectroscopic characterizations (fig. S30), the successful loading of the Fe_2O_3-NiO_xH_y electrocatalyst on a FeF substrate (Fe_2O_3-NiO_xH_y/FeF) was confirmed. To exclude the possible role of NiOOH or NiOOH/FeOOH species during the electrochemical OER tests, FeF electrodes with the Ni oxyhydroxide (NiO_xH_y/FeF) and NiFe oxyhydroxide (NiFeOOH/FeF) composites were also fabricated and evaluated. From Fig. 3A and fig. S31, it is clear that Fe_2O_3-NiO_xH_y/FeF showed a much higher OER activity than the $NiFeO_xH_y$/FeF, NiO_xH_y/FeF and pure FeF counterparts in 1 M KOH, suggesting that the highly efficient OER performance on Fe_2O_3-NiO_xH_y/FeF is mainly originated from the interfaced Fe_2O_3-NiO_xH_y species rather than Fe-doped oxyhydroxides. This further confirms the intrinsic active nature of the Fe_2O_3-NiO_xH_y hybrid electrocatalysts. Because of the highly effective electrode preparation method (see details in Materials and Methods) used to fabricate the active Fe_2O_3-NiO_xH_y species here, the OER activity on the Fe_2O_3-NiO_xH_y/FeF does not decay evidently even with an enlarged surface area (fig. S32), which is of great importance for practical WE applications. Further durability tests demonstrate a prolonged stability on Fe_2O_3-NiO_xH_y/FeF electrode under large current densities (100 mA cm^{-2}), showing negligible changes of OER activity after over 160 hours (fig. S33) that can benefit a robust WE performance.

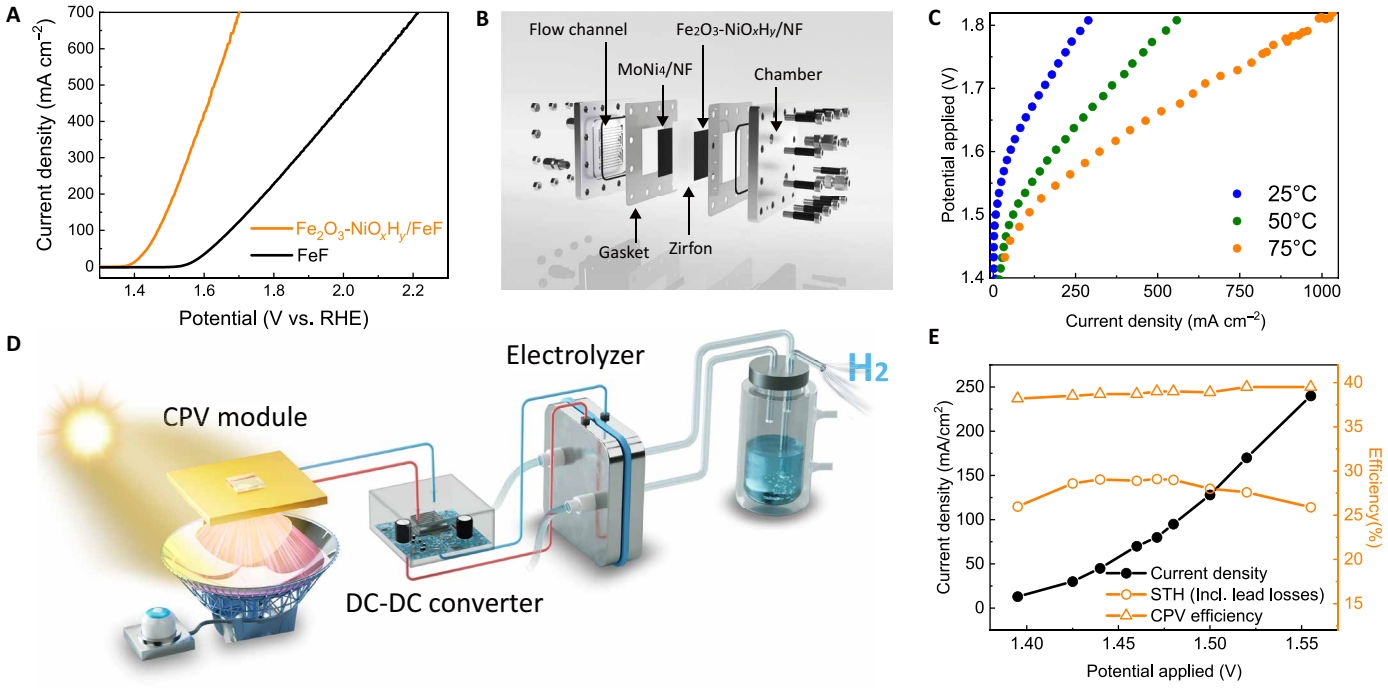

Fig. 3. Electrochemical measurements of Fe_2O_3-NiO_xH_y/FeF electrode and the corresponding WE and PVE performance using the Fe_2O_3-NiO_xH_y/FeF anode. (**A**) OER polarization curves of Fe_2O_3-NiO_xH_y/FeF and pure FeF electrodes in 1 M KOH at a scan rate of 1 mV s^{-1} without *iR* correction. (**B**) Schematic illustration of the zero-gap AWE using Fe_2O_3-NiO_xH_y/FeF and $MoNi_4$/NF as the anode and the cathode (Fe_2O_3-NiO_xH_y/FeF||$MoNi_4$/NF), respectively. (**C**) WE polarization curves of Fe_2O_3-NiO_xH_y/FeF||$MoNi_4$/NF at 25°, 50°, and 75°C in 6 M KOH. (**D**) The schematics of the PVE system consisting of a high-performance Fe_2O_3-NiO_xH_y/FeF||$MoNi_4$/NF zero-gap AWE cell that is electrically coupled with a CPV mini-module through a customized DC-DC converter. The natural sunlight is focused onto a single 1-cm^2 GaInP/GaInAs/Ge triple-junction concentrator cell (mounted on a water-cooled heatsink) via a highly reflective concentrating mirror. The movement of the CPV unit (including the mirror and the solar cell module) is controlled by a sun tracker. (**E**) Measured characteristic *I-V* curves of the PV and electrochemical components (measured separately) of the PVE device, showing the efficiency of CPV and STH processes.

Alkaline WE performance and STH conversion

Using the as-fabricated Fe_2O_3-NiO_xH_y/FeF electrode and the $MoNi_4$/NF materials [prepared according to previous report (*36*)] as the anode and the cathode, respectively, a zero-gap AWE cell is assembled to achieve a high WE performance. As can be seen from Fig. 3C, because of the highly efficient OER performance of Fe_2O_3-NiO_xH_y/FeF, the as-assembled Fe_2O_3-NiO_xH_y/FeF||$MoNi_4$/NF electrolyzer exhibits a remarkably high WE activity in 6 M KOH, reaching a *j* of 280 mA cm^{-2} at 1.8 V. Notably, the robust stability of the Fe_2O_3-NiO_xH_y/FeF electrode endows the Fe_2O_3-NiO_xH_y/FeF||$MoNi_4$/NF electrolyzer a durable WE behavior, showing no evident decay of WE performance over 520 hours (fig. S34). Such an efficient overall WE performance can be further improved under 75°C due to the promoted electrode kinetics and mass transport, delivering a current density of 1 A cm^{-2} at merely 1.8 V, which surpasses most of the alkaline WE technologies reported so far (table S3). Typically, WE is an endothermal process at low overpotential range, while this becomes exothermal at large cell voltages, generating ample amount of heat on the electrodes that might destroy the active species and membranes under ultrahigh current densities (*37*). To this end, taking the external heating may not be necessary and economic to accelerate the WE rate at high voltages. In contrast, under low overpotentials (where a high WE efficiency can be obtained), balancing the energy for an external heating would be important to make a trade-off between overall energy efficiency and WE performance. Therefore, at low voltages (e.g., <2 V), managing an external heating source with the WE process would be more meaningful.

In addition to an enhanced WE performance, the solar cell efficiency and the proper integration between WE and PV components are also crucial for attaining a high overall STH performance at practical current densities (*38*). Among various PV technologies, CPV provides the highest sunlight-to-electricity conversion efficiency under large current densities. Moreover, during operation, ample amount of heat can be generated by CPV modules under concentrated sunlight, which offers opportunities to produce energy or valuable chemicals in a hybrid (e.g., electrical-thermal) system, thereby enabling a capability for power generation near 100% (*39*, *40*). In this regard, electrically and thermally coupling the CPV and AWE units offers great promises to obtain a high-performance PV-WE process (Fig. 3D), as the electrolysis rate can be escalated drastically using the CPV by-product heat that is otherwise detrimental to PV performance (*38*). Thus, to demonstrate the advances of the as-developed electrocatalysts for a high-rate STH conversion, the zero-gap Fe_2O_3-NiO_xH_y/FeF||$MoNi_4$/NF electrolyzer was electrically integrated with a high-performance CPV receiver (consisting of a highly reflective 8-inch-diameter concentrating mirror focusing sunlight onto a single 1-cm^2 GaInP/GaInAs/Ge triple-junction concentrator cell mounted on a water-cooled heatsink), through a customized DC-DC converter (as shown in fig. S35). Because of the limited amount of heat obtained from a 20-W CPV receiver, an external heating source was used to

heat the WE unit to emulate the by-product heat generated from a scaled CPV-WE system (e.g., >1 kW; fig. S36). Impressively, under natural sunlight irradiation (i.e., outdoor testing), the integrated CPV-AWE system can exhibit a STH efficiency as high as 29.1 and 25.9% (refer to 30.3 and 28.9% if the lead losses are subtracted; see details in fig. S37) at a current density of 95 and 240 mA cm^{-2}, respectively, which is the highest among all PV-WE systems reported so far (table S4), outperforming nearly all the state-of-the-art solar-to-X (X = fuels or chemicals) systems. This not only sheds light into the development of efficient WE technologies but also demonstrates feasible strategies in constructing economic solar fuel production approaches.

DISCUSSION

In conclusion, through the development of efficient OER electrocatalysts comprising ultrasmall Fe_2O_3 NPs loaded on a Ni oxyhydroxide substrate, a high-performance AWE cell is fabricated, which substantially enhances the PV-WE activity that in turn benefits superior STH efficiencies. Combined spectroscopic investigations suggested that the high OER performance on the Fe_2O_3-NiO_xH_y catalysts is mainly ascribed to the formation of abundant Fe_2O_3-NiO_xH_y interfaces, where edge Fe atoms and surface Ni sites can act synergistically to enable a bifunctional mechanism, as supported by the computational studies. Constructing such kind of highly active OER catalysts on FeF substrate generates efficient WE anodes that can be readily scaled up for practical AWE process, delivering a WE current density of 1 A cm^{-2} at merely 1.8 V. Further integrating such high-performance AWE unit with a highly efficient CPV module generates a record-breaking high STH efficiency of around 30% at large currents, which surpasses all solar H_2 systems reported so far for practical currents. Hence, through designing the efficient OER electrocatalysts by forming the Fe_2O_3-NiO_xH_y hybrid, the as-demonstrated PV-WE system here not only provides a feasible approach to realize the green H_2 production with cost-effectiveness but also proves the practical efficacy of developing high-rate AWE technology in facilitating the PV-WE process.

MATERIALS AND METHODS

Chemicals

All reaction reagents and chemicals were obtained and used in their as-received form without any further purification. $Ni(NO_3)_2{\cdot}6H_2O$, $Fe(NO_3)_3{\cdot}9H_2O$, Nafion solution (5 weight %), potassium hydroxide, and ethylenediaminetetraacetic acid tetrasodium salt hydrate ($Na_4EDTA{\cdot}xH_2O$) were obtained from Sigma-Aldrich. Deionized (DI) water was obtained through the water purification system (Milli-Q water) in the laboratory. Nickle and iron foam were purchased from Goodfellow and American Elements, respectively. Platinized titanium felt (PTF) was purchased from Fuel Cell Store. The GaInP/GaInAs/Ge-based CPV module was obtained from AZUR SPACE.

Material synthesis

Typically, to prepare the Fe_2O_3-NiO_xH_y/NF, certain amounts of $Fe(NO_3)_3{\cdot}9H_2O$ (4 mM) and $Na_4EDTA{\cdot}xH_2O$ (2 mM) were dissolved into 50 ml of DI water to afford a homogeneous aqueous solution, followed by adding 25 ml of methanol into it. The mixed solution obtained above was then transferred into a Teflon-lined container containing NF substrates and enclosed into a 100-ml stainless steel autoclave followed by heating at 190°C for 3 hours. After the hydrothermal process, the as-obtained Fe_2O_3-NiO_xH_y/NF products were washed with DI water several times to remove possible chemical impurities and dried in oven at 75°C. To characterize the physicochemical properties of ultrasmall Fe_2O_3 NPs, the red precipitates (mainly Fe_2O_3) yielded from the above hydrothermal process were further collected and washed with DI water several times, followed by drying in oven at 75°C. For comparison purpose, NiO_xH_y/NF was also fabricated through the similar hydrothermal method in absence of $Fe(NO_3)_3{\cdot}9H_2O$. Notably, to afford Fe_2O_3-NiO_xH_y/NF sample with large Fe_2O_3 NPs, DI water was adopted to replace the methanol solution during the hydrothermal process. For mechanism studies and WE applications, Fe_2O_3-NiO_xH_y/PTF and Fe_2O_3-NiO_xH_y/FeF were also synthesized by a modified hydrothermal process combined with electrodeposition. For example, through conducting chronoamperometry at −1 V_{SCE} for 1200 s in 600 mM $Ni(NO_3)_2$ solution, a uniform layer of NiO_xH_y was deposited onto the Fe foam skeleton, forming the NiO_xH_y/FeF electrodes. Then, the NiO_xH_y/FeF was transferred into a Teflon-lined container containing a mixed aqueous methanol solution (50 ml of DI water and 25 ml of methanol) with 0.4 M $Fe(NO_3)_3{\cdot}9H_2O$ and 0.2 M $Na_4EDTA{\cdot}xH_2O$, followed by a hydrothermal process in 100-ml stainless steel autoclave at 190°C for 3 hours to afford Fe_2O_3-NiO_xH_y/FeF. To prepare Fe_2O_3-NiO_xH_y/PTF for intrinsic activity studies, a two-step hydrothermal method was adopted. First, 50 ml of aqueous solution containing 5 mM $Ni(NO_3)_2$ and 2.5 mM $Na_4EDTA{\cdot}xH_2O$ was prepared and enclosed into a Teflon-lined autoclave container with PTF substrates. After adding 25 ml of methanol into the above solution, the autoclave was kept at 190°C for 6 hours to afford the NiO_xH_y/PTF electrode. To avoid the formation of possible Fe-doped NiOOH species on NiO_xH_y/PTF, $Ni(NO_3)_2$ with a high purity (99.999%, trace metals basis, Sigma-Aldrich) was used here, while the Teflon-lined container was washed carefully with hydrochloric acid before use. Within the second step, the NiO_xH_y/PTF was put into a 0.5 mM $Fe(NO_3)_3$ solution (50 ml of DI and 25 ml of methanol) containing 0.25 mM $Na_4EDTA{\cdot}xH_2O$, followed by another hydrothermal process for 3 hours at 190°C to yield the Fe_2O_3-NiO_xH_y/PTF. For comparison, Fe_2O_3/PTF was synthesized through a similar procedure in the absence of the first hydrothermal process (formation of NiO_xH_y). $NiFeO_xH_y$ was obtained by directly conducting hydrothermal reaction in an aqueous solution containing both 5 mM $Ni(NO_3)_2$ and 0.5 mM $Fe(NO_3)_3$ (together with 2.75 mM $Na_4EDTA{\cdot}xH_2O$). On the basis of previous report, Fe-incorporated NiO_xH_y was prepared through a Fe-spiking process (*41*). PTF, Ni foam, and Fe foam substrates were all cleaned in ethanol before use with the help of a sonication process for 15 min.

Electrochemical measurement

The electrochemical tests were all performed in 1 M KOH aqueous solution within a three-electrode system at room temperature on a computer-controlled potentiostat (Autolab, PGSTAT204) with current booster (Autolab, Booster 10A). The oxygen evolution activity was investigated by polarization curves with a scan rate of 1 mV s^{-1}. To preclude the influence of Fe impurities, 1 M KOH solution adopted within a three-electrode system was purified using the method in previous reports (*30*). The as-prepared Fe_2O_3-NiO_xH_y/NF, Fe_2O_3-NiO_xH_y/PTF, and Fe_2O_3-NiO_xH_y/FeF were directly used as working electrodes. A graphite rod and mercury/mercury oxide (Hg/HgO) electrode were used as counter and reference electrode, respectively.

All of the obtained potentials were calibrated to a RHE ($E_{RHE} = E_{Hg/HgO} + 0.092 + 0.059 \times pH$) and all current densities were normalized to a geometric surface area. Linear sweep voltammetry for OER was conducted at a scan rate of 1 mV s^{-1} and all the polarization curves were not *iR* corrected. The Tafel slope was calculated using the Tafel equation: $\eta = b \log (j/j_o)$ (η, *b*, *j*, and j_o represent the overpotential, Tafel slope, current density, and exchange current density, respectively), and a scan rate of 1 mV s^{-1} was used to obtain the polarization curves for Tafel plots. The long-term stability tests of OER were performed on the as-prepared self-supported Ni or Fe foam electrode with a surface area of 0.25 cm^2. To study the intrinsic activity of the as-prepared catalysts on PTF substrates, the PTF-based electrodes were immersed into 30% HNO_3 to dissolve the catalysts with a microwave-assisted digestion method. The amount of different metal content in catalysts was lastly determined by inductively coupled plasma–mass spectroscopy (ICP-MS).

Further, the TOF values of the electrocatalysts were calculated from equation as following

$$\mathrm{TOF} = \frac{J \times A \times \eta}{4F \times n} \quad (1)$$

where *J* is obtained at 95% *iR*-corrected overpotential = 300 mV, normalized by geometric area of electrodes (e.g., 0.25 cm^2), and *R* is the series resistance obtained from the fitting of electrochemical impedance spectroscopy. *A* is the geometric area of electrodes (e.g., 0.25 cm^2). *F* is the Faraday constant and η is the Faradaic efficiency. Within this study, Fe edge sites on the Fe_2O_3 were regarded as the active sites that interact strongly with Ni atoms on NiO_xH_y, which form abundant catalytic interface for OER. Therefore, during the TOF evaluation, *n* is adopted as the mole number of iron atoms on the electrode.

In situ Raman measurements were conducted using an electrochemical cell with quartz window (Gooss Union, China), where 0.1 M KOH-$H_2{}^{16}O$ or KOH-$H_2{}^{18}O$ solution was used as electrolyte. During the measurements, each spectrum was recorded at a constant potential until the Raman test is finished.

To perform the WE tests, a Ni-alloy–based electrolyzer (5 × 5 cm^2, Fuel Cell Store) with serpentine flow channels was used. During the WE experiments, the Fe_2O_3-NiO_xH_y/FeF was directly used as the OER anode, while a $MoNi_4$/NF was prepared according to previously reported method was adopted as the HER cathode (*36*). To evaluate the alkaline WE performance of Fe_2O_3-NiO_xH_y/FeF electrode under industrial conditions, the electrochemical measurements within such AW device were carried out in 6 M KOH solution at different temperatures with external heating.

Within a CPV-AWE system, the STH efficiency was evaluated carefully using a linear product of three elemental efficiencies as below

$$\mathrm{STH} = \eta_{CPV}\eta_{DCDC}\eta_{EC} = \left(\frac{P_{CPV\ out}}{P_{irradiation}}\right)\left(\frac{P_{DCDC\ out}}{P_{DCDC\ in}}\right)\left(\frac{I_{EC} * 1.23V}{P_{EC\ in}}\right) \quad (2)$$

where DCDC refers to the DCDC converter connecting the CPV and AWE. The difference between $P_{CPV\ out}$ and $P_{DCDC\ in}$ is due to lead resistance (I^2R) loss, as is the difference between $P_{DCDC\ out}$ and $P_{EC\ in}$. The AW performance can be monitored simultaneously through integrated detection probe. During the measurements, the sun tracker was kept under alignment with sunlight while mirror was concentrating the sunlight on CPV module (Azur Space, 3C44 triple junction). An iris aperture on mirror was used to control the sunlight incident. This experiment is conducted under real sunlight, so the inlet irradiation could be slightly affected by clouds and celestial movement. An alignment check (to ensure full capture of the concentrated sunlight inside the CPV cell active area) and irradiation calibration were performed before and after every test.

Limited by the small scale of setup (e.g., up to 20 W for CPV device), the heat generated by the AWE and CPV module is not enough to warm up the AWE unit. Therefore, an external circulating water heating system (e.g., temperature-controlled water bath) is used to maintain the AWE temperature (e.g., 80°C). Four resistance temperature detectors were used to monitor the AWE temperature including electrolyte in, electrolyte out, cathode body, and anode body. A separate temperature-controlled bath was used to maintain the CPV solar cell temperature, affixed to a heatsink, at 25°C. The efficiency of the CPV receiver was typically 39% at the highest concentrations measured.

Physicochemical characterizations

TEM was carried out on a Phillips/CM 200 microscope operated at an accelerating voltage of 200 kV. SEM was conducted on a JEOL 7001F operated at 5 kV. XPS measurements were carried out on a Thermo ESCALAB250Xi x-ray photoelectron spectrometer using Cu Kα x-rays as the excitation source with a voltage of 12.5 kV and power of 250 W. HAADF-STEM and energy-dispersive x-ray mapping were obtained on a spherical aberration-corrected transmission electron microscope (FEI Titan G2 80-200), which was operated at 200 kV. Fe K-edge XAS measurements were performed on the beamline 17C1 (BL17C1) at the National Synchrotron Radiation Research Center (NSRRC, Taiwan). Data were collected using a fluorescence geometry and scanned from 200 eV below the Fe K-edge (7709 eV) to ~1000 eV past the edge. Multiple scans (six times) were averaged to improve the signal-to-noise ratio. Data reduction and subsequent modeling efforts were performed using the Demeter software package (*42*). Modeling results used a Fe_2O_3 cluster (materials project ID: mp-565814) to model Fe-O and Fe-Fe backscattering paths. An $S_0{}^2$ value of 0.776 was used for all models and obtained from modeling a reference Fe foil. ICP-MS was carried out using a PerkinElmer quadrapole Nexion instrument. O K-edge, Ni L-edge, and Fe L-edge NEXAFS spectroscopy measurements were collected at a 55° angle of incidence in a vacuum chamber with a base pressure of 10^{-7} mbar on the soft x-ray beamline at the Australian Synchrotron, ANSTO. The signals were acquired in total electron yield mode and the data were processed using the program called QANT.

DFT calculations

DFT + U was used to carry out free energies calculations using the Vinenna Ab initio Simulation Package code (*43*, *44*). The electron correlation functional was used through the generalized gradient approximation in the form of Perdew-Burke-Ernzerhof (*45*). The dispersion interaction was considered by using DFT + D3 semiempirical correction in Grimme's scheme (*46*). Blöchl's all-electron, frozen-core projector-augmented wave method was chosen to describe ion-electron interactions (*47*, *48*). In case of geometrical optimization, the convergence tolerances of displacement, force, and energy were set to 5×10^{-3} Å, 5×10^{-3} eV $Å^{-1}$, and 10^{-5} eV, respectively. To determine the trend of OER, Hubbard *U* values of 4.3 and 3.8 eV were used for Fe and Ni atoms, respectively (*49*, *50*). For all the structures, a vacuum gap of 15 Å was used in the *z*-direction to remove the spurious layer interactions. In this system, (110) surface of

hametite was chosen as it is reported to be more OER active phase (*51*). A slab of four layers for hematite was used for the calculations.

The complete OER process can be described as the following equation (*52*)

$$2H_2O(l) \rightarrow O_2(g) + 4e^- + 4H^+ \quad (3)$$

It consists of four elementary steps, also known as four-electron steps

$$H_2O(l) + {}^* \rightarrow OH^* + e^- + H^+ \quad (4)$$

$$OH^* \rightarrow O^* + e^- + H^+ \quad (5)$$

$$O^* + H_2O(l) \rightarrow OOH^* + e^- + H^* \quad (6)$$

$$OOH^* \rightarrow O_2(g) + e^- + H^+ \quad (7)$$

where * represents one activated site, and *l* and *g* represent the liquid and gas phases, respectively.

The calculation method to calculate the Gibbs free-energy difference for each step as proposed by Nørskov *et al.* was used and is given as (*14*)

$$\Delta G = \Delta E + \Delta \mathrm{ZPE} - T\Delta S + \Delta G_U + \Delta G_{\mathrm{pH}} \quad (8)$$

where ΔE is the electronic energy change and can be obtained directly from the DFT calculations, ΔZPE is the change of zero-point energy, T is the temperature and (298.15 K), and ΔS is the change in entropy of products and reactants. $\Delta G_U = -eU$ is the contribution of electrode potential to free energy change, and $\Delta G_{\mathrm{pH}} = -k_{\mathrm{B}}T\ln 10 \times \mathrm{pH}$.

Supplementary Materials

This PDF file includes:

Figs. S1 to S37
Tables S1 to S4
References

REFERENCES AND NOTES

1. J. F. Geisz, R. M. France, K. L. Schulte, M. A. Steiner, A. G. Norman, H. L. Guthrey, M. R. Young, T. Song, T. Moriarty, Six-junction III–V solar cells with 47.1% conversion efficiency under 143 Suns concentration. *Nat. Energy* **5**, 326–335 (2020).
2. Z. Y. Yu, Y. Duan, X. Y. Feng, X. Yu, M. R. Gao, S. H. Yu, Clean and affordable hydrogen fuel from alkaline water splitting: Past, recent progress, and future prospects. *Adv. Mater.* **33**, e2007100 (2021).
3. H. Xie, Z. Zhao, T. Liu, Y. Wu, C. Lan, W. Jiang, L. Zhu, Y. Wang, D. Yang, Z. Shao, A membrane-based seawater electrolyser for hydrogen generation. *Nature* **612**, 673–678 (2022).
4. A. Hodges, A. L. Hoang, G. Tsekouras, K. Wagner, C.-Y. Lee, G. F. Swiegers, G. G. Wallace, A high-performance capillary-fed electrolysis cell promises more cost-competitive renewable hydrogen. *Nat. Commun.* **13**, 1304 (2022).
5. L. Wan, M. Pang, J. Le, Z. Xu, H. Zhou, Q. Xu, B. Wang, Oriented intergrowth of the catalyst layer in membrane electrode assembly for alkaline water electrolysis. *Nat. Commun.* **13**, 7956 (2022).
6. Y. Bai, Y. Wu, X. Zhou, Y. Ye, K. Nie, J. Wang, M. Xie, Z. Zhang, Z. Liu, T. Cheng, C. Gao, Promoting nickel oxidation state transitions in single-layer NiFeB hydroxide nanosheets for efficient oxygen evolution. *Nat. Commun.* **13**, 6094 (2022).
7. Z. W. Seh, J. Kibsgaard, C. F. Dickens, I. Chorkendorff, J. K. Nørskov, T. F. Jaramillo, Combining theory and experiment in electrocatalysis: Insights into materials design. *Science* **355**, eaad4998 (2017).
8. B. Zhang, X. Zheng, O. Voznyy, R. Comin, M. Bajdich, M. García-Melchor, L. Han, J. Xu, M. Liu, L. Zheng, F. P. García de Arquer, C. T. Dinh, F. Fan, M. Yuan, E. Yassitepe, N. Chen, T. Regier, P. Liu, Y. Li, P. De Luna, A. Janmohamed, H. L. Xin, H. Yang, A. Vojvodic, E. H. Sargent, Homogeneously dispersed multimetal oxygen-evolving catalysts. *Science* **352**, 333–337 (2016).
9. F. Song, X. Hu, Exfoliation of layered double hydroxides for enhanced oxygen evolution catalysis. *Nat. Commun.* **5**, 4477 (2014).
10. Z. Huang, J. Song, Y. Du, S. Xi, S. Dou, J. M. V. Nsanzimana, C. Wang, Z. J. Xu, X. Wang, Chemical and structural origin of lattice oxygen oxidation in Co–Zn oxyhydroxide oxygen evolution electrocatalysts. *Nat. Energy* **4**, 329–338 (2019).
11. C. Roy, B. Sebok, S. B. Scott, E. M. Fiordaliso, J. E. Sørensen, A. Bodin, D. B. Trimarco, C. D. Damsgaard, P. C. K. Vesborg, O. Hansen, I. E. L. Stephens, J. Kibsgaard, I. Chorkendorff, Impact of nanoparticle size and lattice oxygen on water oxidation on $NiFeO_xH_y$. *Nat. Catal.* **1**, 820–829 (2018).
12. F. Dionigi, Z. Zeng, I. Sinev, T. Merzdorf, S. Deshpande, M. B. Lopez, S. Kunze, I. Zegkinoglou, H. Sarodnik, D. Fan, A. Bergmann, J. Drnec, J. F. de Araujo, M. Gliech, D. Teschner, J. Zhu, W.-X. Li, J. Greeley, B. R. Cuenya, P. Strasser, In-situ structure and catalytic mechanism of NiFe and CoFe layered double hydroxides during oxygen evolution. *Nat. Commun.* **11**, 2522 (2020).
13. G. Shen, R. Zhang, L. Pan, F. Hou, Y. Zhao, Z. Shen, W. Mi, C. Shi, Q. Wang, X. Zhang, J.-J. Zou, Regulating the spin state of Fe^{III} by atomically anchoring on ultrathin titanium dioxide for efficient oxygen evolution electrocatalysis. *Angew. Chem. Int. Ed. Engl.* **59**, 2313–2317 (2020).
14. H. Wu, T. Yang, Y. Du, L. Shen, G. W. Ho, Identification of facet-governing reactivity in hematite for oxygen evolution. *Adv. Mater.* **30**, e1804341 (2018).
15. M. C. Toroker, Theoretical insights into the mechanism of water oxidation on nonstoichiometric and titanium-doped Fe_2O_3(0001). *J. Phys. Chem. C* **118**, 23162–23167 (2014).
16. Z. Xiao, Y. C. Huang, C. L. Dong, C. Xie, Z. Liu, S. Du, W. Chen, D. Yan, L. Tao, Z. Shu, G. Zhang, H. Duan, Y. Wang, Y. Zou, R. Chen, S. Wang, Operando identification of the dynamic behavior of oxygen vacancy-rich Co_3O_4 for oxygen evolution reaction. *J. Am. Chem. Soc.* **142**, 12087–12095 (2020).
17. F. Frati, M. O. J. Y. Hunault, F. M. F. de Groot, Oxygen k-edge x-ray absorption spectra. *Chem. Rev.* **120**, 4056–4110 (2020).
18. T. Park, S. Sambasivan, D. A. Fischer, W.-S. Yoon, J. A. Misewich, S. S. Wong, Electronic structure and chemistry of iron-based metal oxide nanostructured materials: A NEXAFS investigation of $BiFeO_3$, $Bi_2Fe_4O_9$, α-Fe_2O_3, γ-Fe_2O_3, and Fe/Fe_3O_4. *J. Phys. Chem. C* **112**, 10359–10369 (2008).
19. J. Zhang, Z. Y. Wu, K. Ibrahim, M. I. Abbas, X. Ju, Surface structure of α-Fe_2O_3 nanocrystal observed by O K-edge X-ray absorption spectroscopy. *Nucl. Instrum. Methods Phys. Res. B* **199**, 291–294 (2003).
20. T. Ling, P. Da, X. Zheng, B. Ge, Z. Hu, M. Wu, X.-W. Du, W.-B. Hu, M. Jaroniec, S.-Z. Qiao, Atomic-level structure engineering of metal oxides for high-rate oxygen intercalation pseudocapacitance. *Sci. Adv.* **4**, eaau6261 (2018).
21. Y. Zhang, Y. Hu, Z. Wang, T. Lin, X. Zhu, B. Luo, H. Hu, W. Xing, Z. Yan, L. Wang, Lithiation-induced vacancy engineering of Co_3O_4 with improved faradic reactivity for high-performance supercapacitor. *Adv. Funct. Mater.* **30**, 2004172 (2020).
22. B. J. Trześniewski, O. Diaz-Morales, D. A. Vermaas, A. Longo, W. Bras, M. T. M. Koper, W. A. Smith, In situ observation of active oxygen species in Fe-containing Ni-based oxygen evolution catalysts: The effect of pH on electrochemical activity. *J. Am. Chem. Soc.* **137**, 15112–15121 (2015).
23. T. Sharifi, E. Gracia-Espino, H. Reza Barzegar, X. Jia, F. Nitze, G. Hu, P. Nordblad, C.-W. Tai, T. Wågberg, Formation of nitrogen-doped graphene nanoscrolls by adsorption of magnetic γ-Fe_2O_3 nanoparticles. *Nat. Commun.* **4**, 2319 (2013).
24. D. L. A. de Faria, S. Venâncio Silva, M. T. de Oliveira, Raman microspectroscopy of some iron oxides and oxyhydroxides. *J. Raman Spectrosc.* **28**, 873–878 (1997).
25. L. Bai, S. Lee, X. Hu, Spectroscopic and electrokinetic evidence for a bifunctional mechanism of the oxygen evolution reaction. *Angew. Chem. Int. Ed. Engl.* **60**, 3095–3103 (2020).
26. S. Lee, K. Banjac, M. Lingenfelder, X. Hu, Oxygen isotope labeling experiments reveal different reaction sites for the oxygen evolution reaction on nickel and nickel iron oxides. *Angew. Chem. Int. Ed. Engl.* **58**, 10295–10299 (2019).
27. Z. He, J. Zhang, Z. Gong, H. Lei, D. Zhou, N. Zhang, W. Mai, S. Zhao, Y. Chen, Activating lattice oxygen in NiFe-based (oxy)hydroxide for water electrolysis. *Nat. Commun.* **13**, 2191 (2022).
28. S. Lee, L. Bai, X. Hu, Deciphering iron-dependent activity in oxygen evolution catalyzed by nickel–iron layered double hydroxide. *Angew. Chem. Int. Ed. Engl.* **59**, 8072–8077 (2020).
29. D. Friebel, M. W. Louie, M. Bajdich, K. E. Sanwald, Y. Cai, A. M. Wise, M.-J. Cheng, D. Sokaras, T.-C. Weng, R. Alonso-Mori, R. C. Davis, J. R. Bargar, J. K. Nørskov, A. Nilsson, A. T. Bell, Identification of highly active Fe sites in (Ni,Fe)OOH for electrocatalytic water splitting. *J. Am. Chem. Soc.* **137**, 1305–1313 (2015).
30. L. Trotochaud, S. L. Young, J. K. Ranney, S. W. Boettcher, Nickel–iron oxyhydroxide oxygen-evolution electrocatalysts: The role of intentional and incidental iron incorporation. *J. Am. Chem. Soc.* **136**, 6744–6753 (2014).
31. J. Rossmeisl, A. Logadottir, J. K. Nørskov, Electrolysis of water on (oxidized) metal surfaces. *Chem. Phys.* **319**, 178–184 (2005).
32. D. R. Kauffman, X. Deng, D. C. Sorescu, T.-D. Nguyen-Phan, C. Wang, C. M. Marin, E. Stavitski, I. Waluyo, A. Hunt, Edge-enhanced oxygen evolution reactivity at ultrathin, Au-supported Fe_2O_3 electrocatalysts. *ACS Catal.* **9**, 5375–5382 (2019).

33. K. George, X. Zhang, A. Bieberle-Hütter, Why does NiOOH cocatalyst increase the oxygen evolution activity of α-Fe_2O_3? *J. Chem. Phys.* **150**, 041729 (2019).
34. B. H. R. Suryanto, Y. Wang, R. K. Hocking, W. Adamson, C. Zhao, Overall electrochemical splitting of water at the heterogeneous interface of nickel and iron oxide. *Nat. Commun.* **10**, 5599 (2019).
35. Z.-W. Gao, J.-Y. Liu, X.-M. Chen, X.-L. Zheng, J. Mao, H. Liu, T. Ma, L. Li, W.-C. Wang, X.-W. Du, Engineering NiO/NiFe LDH intersection to bypass scaling relationship for oxygen evolution reaction via dynamic tridimensional adsorption of intermediates. *Adv. Mater.* **31**, e1804769 (2019).
36. J. Zhang, T. Wang, P. Liu, Z. Liao, S. Liu, X. Zhuang, M. Chen, E. Zschech, X. Feng, Efficient hydrogen production on $MoNi_4$ electrocatalysts with fast water dissociation kinetics. *Nat. Commun.* **8**, 15437 (2017).
37. F. Yang, M. J. Kim, M. Brown, B. J. Wiley, Alkaline water electrolysis at 25 A cm^{-2} with a microfibrous flow-through electrode. *Adv. Energy Mater.* **10**, 2001174 (2020).
38. S. Tembhurne, F. Nandjou, S. Haussener, A thermally synergistic photo-electrochemical hydrogen generator operating under concentrated solar irradiation. *Nat. Energy* **4**, 399–407 (2019).
39. M. Roeb, H. Müller-Steinhagen, Concentrating on solar electricity and fuels. *Science* **329**, 773–774 (2010).
40. I. Holmes-Gentle, S. Tembhurne, C. Suter, S. Haussener, Kilowatt-scale solar hydrogen production system using a concentrated integrated photoelectrochemical device. *Nat. Energy* **8**, 586–596 (2023).
41. M. B. Stevens, C. D. M. Trang, L. J. Enman, J. Deng, S. W. Boettcher, Reactive Fe-sites in Ni/Fe (Oxy)hydroxide are responsible for exceptional oxygen electrocatalysis activity. *J. Am. Chem. Soc.* **139**, 11361–11364 (2017).
42. B. Ravel, M. Newville, ATHENA, ARTEMIS, HEPHAESTUS: Data analysis for X-ray absorption spectroscopy using IFEFFIT. *J. Synchrotron Radiat.* **12**, 537–541 (2005).
43. G. Kresse, J. Furthmüller, Efficient iterative schemes for *ab initio* total-energy calculations using a plane-wave basis set. *Phys. Rev. B Condens. Matter* **54**, 11169–11186 (1996).
44. G. Kresse, J. Furthmüller, Efficiency of ab-initio total energy calculations for metals and semiconductors using a plane-wave basis set. *Comput. Mater. Sci.* **6**, 15–50 (1996).
45. J. P. Perdew, K. Burke, M. Ernzerhof, Generalized gradient approximation made simple. *Phys. Rev. Lett.* **77**, 3865–3868 (1996).
46. S. Grimme, Semiempirical GGA-type density functional constructed with a long-range dispersion correction. *J. Comput. Chem.* **27**, 1787–1799 (2006).
47. P. E. Blöchl, Projector augmented-wave method. *Phys. Rev. B* **50**, 17953–17979 (1994).
48. G. Kresse, D. Joubert, From ultrasoft pseudopotentials to the projector augmented-wave method. *Phys. Rev. B* **59**, 1758–1775 (1999).
49. P. Liao, J. A. Keith, E. A. Carter, Water oxidation on pure and doped hematite (0001) surfaces: Prediction of Co and Ni as effective dopants for electrocatalysis. *J. Am. Chem. Soc.* **134**, 13296–13309 (2012).
50. N. Alidoust, M. C. Toroker, J. A. Keith, E. A. Carter, Significant reduction in NiO band gap upon formation of $Li_xNi_{1-x}O$ alloys: Applications to solar energy conversion. *ChemSusChem* **7**, 195–201 (2014).
51. S. Kment, P. Schmuki, Z. Hubicka, L. Machala, R. Kirchgeorg, N. Liu, L. Wang, K. Lee, J. Olejnicek, M. Cada, I. Gregora, R. Zboril, Photoanodes with fully controllable texture: The enhanced water splitting efficiency of thin hematite films exhibiting solely (110) crystal orientation. *ACS Nano* **9**, 7113–7123 (2015).
52. J. K. Nørskov, J. Rossmeisl, A. Logadottir, L. Lindqvist, J. R. Kitchin, T. Bligaard, H. Jónsson, Origin of the overpotential for oxygen reduction at a fuel-cell cathode. *J. Phys. Chem. B* **108**, 17886–17892 (2004).
53. L. Zhuang, L. Ge, Y. Yang, M. Li, Y. Jia, X. Yao, Z. Zhu, Ultrathin iron-cobalt oxide nanosheets with abundant oxygen vacancies for the oxygen evolution reaction. *Adv. Mater.* **29**, 1606793 (2017).
54. L. Gong, X. Y. E. Chng, Y. Du, S. Xi, B. S. Yeo, Enhanced catalysis of the electrochemical oxygen evolution reaction by iron(III) ions adsorbed on amorphous cobalt oxide. *ACS Catal.* **8**, 807–814 (2018).
55. Y. Lin, J. Fang, W. Wang, Q. Wen, D. Huang, D. Ding, Z. Li, Y. Liu, Y. Shen, T. Zhai, Operando reconstructed molecule fence to stabilize NiFe-based oxygen evolution catalysts. *Adv. Energy Mater.* **13**, 2300604 (2023).
56. H. Wang, H.-W. Lee, Y. Deng, Z. Lu, P.-C. Hsu, Y. Liu, D. Lin, Y. Cui, Bifunctional non-noble metal oxide nanoparticle electrocatalysts through lithium-induced conversion for overall water splitting. *Nat. Commun.* **6**, 7261 (2015).
57. H. Yang, L. Gong, H. Wang, C. Dong, J. Wang, K. Qi, H. Liu, X. Guo, B. Y. Xia, Preparation of nickel-iron hydroxides by microorganism corrosion for efficient oxygen evolution. *Nat. Commun.* **11**, 5075 (2020).
58. K. Wang, H. Du, S. He, L. Liu, K. Yang, J. Sun, Y. Liu, Z. Du, L. Xie, W. Ai, W. Huang, Kinetically controlled, scalable synthesis of γ-FeOOH nanosheet arrays on nickel foam toward efficient oxygen evolution: The key role of in-situ-generated γ-NiOOH. *Adv. Mater.* **33**, e2005587 (2021).
59. Q. Qian, Y. Li, Y. Liu, L. Yu, G. Zhang, Ambient fast synthesis and active sites deciphering of hierarchical foam-like trimetal–Organic framework nanostructures as a platform for highly efficient oxygen evolution electrocatalysis. *Adv. Mater.* **31**, e1901139 (2019).
60. H. Liao, T. Luo, P. Tan, K. Chen, L. Lu, Y. Liu, M. Liu, J. Pan, Unveiling role of sulfate ion in nickel-iron (oxy)hydroxide with enhanced oxygen-evolving performance. *Adv. Funct. Mater.* **31**, 2102772 (2021).
61. S. Li, B. Chen, Y. Wang, M.-Y. Ye, P. A. van Aken, C. Cheng, A. Thomas, Oxygen-evolving catalytic atoms on metal carbides. *Nat. Mater.* **20**, 1240–1247 (2021).
62. H. Koshikawa, H. Murase, T. Hayashi, K. Nakajima, H. Mashiko, S. Shiraishi, Y. Tsuji, Single nanometer-sized NiFe-layered double hydroxides as anode catalyst in anion exchange membrane water electrolysis cell with energy conversion efficiency of 74.7% at 1.0 A cm^{-2}. *ACS Catal.* **10**, 1886–1893 (2020).
63. D. Li, W. Wan, Z. Wang, H. Wu, S. Wu, T. Jiang, G. Cai, C. Jiang, F. Ren, Self-derivation and surface reconstruction of Fe-doped Ni_3S_2 electrode realizing high-efficient and stable overall water and urea electrolysis. *Adv. Energy Mater.* **12**, 2201913 (2022).
64. I. Ahmad, J. Ahmed, S. Batool, M. N. Zafar, A. Hanif, Zahidullah, M. F. Nazar, A. Ul-Hamid, U. Jabeen, A. Dahshan, M. Idrees, S. A. Shehzadi, Design and fabrication of Fe_2O_3/FeP heterostructure for oxygen evolution reaction electrocatalysis. *J. Alloys Compd.* **894**, 162409 (2022).
65. R. Zhang, L. Pan, B. Guo, Z.-F. Huang, Z. Chen, L. Wang, X. Zhang, Z. Guo, W. Xu, K. P. Loh, J.-J. Zou, Tracking the role of defect types in Co_3O_4 structural evolution and active motifs during oxygen evolution reaction. *J. Am. Chem. Soc.* **145**, 2271–2281 (2023).
66. H. Zhong, X. Wang, G. Sun, Y. Tang, S. Tan, Q. He, J. Zhang, T. Xiong, C. Diao, Z. Yu, S. Xi, W. S. V. Lee, J. Xue, Optimization of oxygen evolution activity by tuning e^*_g band broadening in nickel oxyhydroxide. *Energ. Environ. Sci.* **16**, 641–652 (2023).
67. L. Wen, X. Zhang, J. Liu, X. Li, C. Xing, X. Lyu, W. Cai, W. Wang, Y. Li, Cr-dopant induced breaking of scaling relations in CoFe layered double hydroxides for improvement of oxygen evolution reaction. *Small* **15**, e1902373 (2019).
68. H. Sun, C. Tian, G. Fan, J. Qi, Z. Liu, Z. Yan, F. Cheng, J. Chen, C.-P. Li, M. Du, Boosting activity on Co_4N porous nanosheet by coupling CeO_2 for efficient electrochemical overall water splitting at high current densities. *Adv. Funct. Mater.* **30**, 1910596 (2020).
69. Y. Song, J. Cheng, J. Liu, Q. Ye, X. Gao, J. Lu, Y. Cheng, Modulating electronic structure of cobalt phosphide porous nanofiber by ruthenium and nickel dual doping for highly-efficiency overall water splitting at high current density. *Appl. Catal. Environ.* **298**, 120488 (2021).
70. D. Wu, D. Chen, J. Zhu, S. Mu, Ultralow Ru incorporated amorphous cobalt-based oxides for high-current-density overall water splitting in alkaline and seawater media. *Small* **17**, e2102777 (2021).
71. H. Chen, H.-B. Huang, H.-H. Li, S.-Z. Zhao, L.-D. Wang, J. Zhang, S.-L. Zhong, C.-F. Lao, L.-M. Cao, C.-T. He, Self-supporting Co/CeO_2 heterostructures for ampere-level current density alkaline water electrolysis. *Inorg. Chem.* **62**, 3297–3304 (2023).
72. M. R. Kraglund, M. Carmo, G. Schiller, S. A. Ansar, D. Aili, E. Christensen, J. O. Jensen, Ion-solvating membranes as a new approach towards high rate alkaline electrolyzers. *Energy Environ. Sci.* **12**, 3313–3318 (2019).
73. J. Kang, G. Liu, Q. Hu, Y. Huang, L. M. Liu, L. Dong, G. Teobaldi, L. Guo, Parallel nanosheet arrays for industrial oxygen production. *J. Am. Chem. Soc.* **145**, 25143–25149 (2023).
74. N. V. Kuleshov, V. N. Kuleshov, S. A. Dovbysh, S. A. Grigoriev, S. V. Kurochkin, P. Millet, Development and performances of a 0.5 kW high-pressure alkaline water electrolyser. *Int. J. Hydrogen Energy* **44**, 29441–29449 (2019).
75. H. I. Lee, M. Mehdi, S. K. Kim, H. S. Cho, M. J. Kim, W. C. Cho, Y. W. Rhee, C. H. Kim, Advanced Zirfon-type porous separator for a high-rate alkaline electrolyser operating in a dynamic mode. *J. Memb. Sci.* **616**, 118541 (2020).
76. A. Alam, C. Park, J. Lee, H. Ju, Comparative analysis of performance of alkaline water electrolyzer by using porous separator and ion-solvating polybenzimidazole membrane. *Renew. Energy* **166**, 222–233 (2020).
77. S. Kim, J. H. Han, J. Yuk, S. Kim, Y. Song, S. So, K. T. Lee, T. H. Kim, Highly selective porous separator with thin skin layer for alkaline water electrolysis. *J. Power Sources* **524**, 231059 (2022).
78. G. Peharz, F. Dimroth, U. Wittstadt, Solar hydrogen production by water splitting with a conversion efficiency of 18%. *Int. J. Hydrogen Energy* **32**, 3248–3252 (2007).
79. S. Licht, B. Wang, S. Mukerji, T. Soga, M. Umeno, H. Tributsch, Efficient solar water splitting, exemplified by RuO_2-catalyzed AlGaAs/Si photoelectrolysis. *J. Phys. Chem. B* **104**, 8920–8924 (2000).
80. O. Khaselev, J. A. Turner, A monolithic photovoltaic-photoelectrochemical device for hydrogen production via water splitting. *Science* **280**, 425–427 (1998).
81. O. Khaselev, High-efficiency integrated multijunction photovoltaic/electrolysis systems for hydrogen production. *Int. J. Hydrogen Energy* **26**, 127–132 (2001).
82. A. Nakamura, Y. Ota, K. Koike, Y. Hidaka, K. Nishioka, M. Sugiyama, K. Fujii, A 24.4% solar to hydrogen energy conversion efficiency by combining concentrator photovoltaic modules and electrochemical cells. *Appl. Phys. Express* **8**, 107101 (2015).

83. J. Jia, L. C. Seitz, J. D. Benck, Y. Huo, Y. Chen, J. W. D. Ng, T. Bilir, J. S. Harris, T. F. Jaramillo, Solar water splitting by photovoltaic-electrolysis with a solar-to-hydrogen efficiency over 30%. *Nat. Commun.* **7**, 13237 (2016).
84. S. M. Bashir, M. A. Nadeem, M. Al-Oufi, M. Al-Hakami, T. T. Isimjan, H. Idriss, Sixteen percent solar-to-hydrogen efficiency using a power-matched alkaline electrolyzer and a high concentrated solar cell: Effect of operating parameters. *ACS Omega* **5**, 10510–10518 (2020).
85. Z. N. Zahran, Y. Miseki, E. A. Mohamed, Y. Tsubonouchi, K. Makita, T. Sugaya, K. Sayama, M. Yagi, Perfect matching factor between a customized double-junction GaAs photovoltaic device and an electrolyzer for efficient solar water splitting. *ACS Appl. Energy Mater.* **5**, 8241–8253 (2022).
86. A. M. K. Fehr, A. Agrawal, F. Mandani, C. L. Conrad, Q. Jiang, S. Y. Park, O. Alley, B. Li, S. Sidhik, I. Metcalf, C. Botello, J. L. Young, J. Even, J. C. Blancon, T. G. Deutsch, K. Zhu, S. Albrecht, F. M. Toma, M. Wong, A. D. Mohite, Integrated halide perovskite photoelectrochemical cells with solar-driven water-splitting efficiency of 20.8%. *Nat. Commun.* **14**, 3797 (2023).
87. H. Chen, L. Song, S. Ouyang, J. Wang, J. Lv, J. Ye, Co and Fe codoped $WO_{2.72}$ as alkaline-solution-available oxygen evolution reaction catalyst to construct photovoltaic water splitting system with solar-to-hydrogen efficiency of 16.9%. *Adv. Sci.* **6**, 1900465 (2019).
88. S. A. Bonke, M. Wiechen, D. R. MacFarlane, L. Spiccia, Renewable fuels from concentrated solar power: Towards practical artificial photosynthesis. *Energy Environ. Sci.* **8**, 2791–2796 (2015).
89. Y. Wang, A. Sharma, T. Duong, H. Arandiyan, T. Zhao, D. Zhang, Z. Su, M. Garbrecht, F. J. Beck, S. Karuturi, C. Zhao, K. Catchpole, Direct solar hydrogen generation at 20% efficiency using low-cost materials. *Adv. Energy Mater.* **11**, 2101053 (2021).
90. S. Niu, W. J. Jiang, Z. Wei, T. Tang, J. Ma, J. S. Hu, L. J. Wan, Se-doping activates FeOOH for cost-effective and efficient electrochemical water oxidation. *J. Am. Chem. Soc.* **141**, 7005–7013 (2019).
91. J. Luo, J.-H. Im, M. T. Mayer, M. Schreier, M. K. Nazeeruddin, N.-G. Park, S. D. Tilley, H. J. Fan, M. Gratzel, Water photolysis at 12.3% efficiency via perovskite photovoltaics and Earth-abundant catalysts. *Science* **345**, 1593–1596 (2014).
92. T. J. Jacobsson, V. Fjällström, M. Sahlberg, M. Edoff, T. Edvinsson, A monolithic device for solar water splitting based on series interconnected thin film absorbers reaching over 10% solar-to-hydrogen efficiency. *Energy Environ. Sci.* **6**, 3676–3683 (2013).

Acknowledgments: We thank UNSW Mark Wainwright Analytical Center for providing access to the SEM, TEM, Raman, XPS, and other facilities. We thank B. Gong from MWAC for the XPS measurements. We also thank D. Mitchell from the University of Wollongong Electron Microscopy Centre for the assistance in HAADF-STEM measurements. **Funding:** The work was supported by the Australian Renewable Energy Agency (ARENA 2018/RND014), the Australian Research Council (ARC) under the Discovery Early Career Researcher Award DE190100131, and ARC Training Centre for Global Hydrogen Economy (IC20010023). X.L. acknowledges the UNSW Scientia Scheme for financial support. Q.Z. acknowledges the National Natural Science Fund for Excellent Young Scientists Fund Program (overseas, no. 04002350153) and the Fundamental Research Funds for the Central Universities (nos. 04002150133 and 0400219013/011) for financial support of the work. **Author contributions:** R.A. and X.L directed the project. R.A., X.L., and Q.Z. conceived the concept. R.A., X.L., and Q.Z. designed the experiments. Q.Z. carried out all the experiments. Y.S. carried out the electrolyzer and PV electrolysis measurements. J.P. built the PV electrolysis system. P.K. and G.K. conducted the computational simulations. M.J.K. and I.P.-W. assisted the PV electrolysis measurements and the design of PV electrolysis devices. M.J.K., J.L., R.D., K.G., and M.A.G. designed the CPV module and contributed to data analysis and manuscript editing. L.T., J.J., K.-H.W., and C.C. performed the XAS experiments and analysis of the data. S.C. performed the HRTEM measurements and analysis. R.A., X.L., Y.S., and Q.Z. analyzed the data. R.A., X.L., Y.S., and Q.Z. co-wrote the manuscript. All authors discussed the results and assisted with the manuscript preparation. **Competing interests:** The authors declare that they have no competing interests. **Data and materials availability:** All data needed to evaluate the conclusions in the paper are present in the paper and/or the Supplementary Materials.

Submitted 29 July 2024
Accepted 24 January 2025
Published 26 February 2025
10.1126/sciadv.ads0836

ScienceAdvances

A photovoltaic-electrolysis system with high solar-to-hydrogen efficiency under practical current densities

Qingran Zhang, Yihao Shan, Jian Pan, Priyank Kumar, Mark J. Keevers, John Lasich, Gurpreet Kour, Rahman Daiyan, Ivan Perez-Wurf, Lars Thomsen, Soshan Cheong, Junjie Jiang, Kuang-Hsu Wu, Chao-Lung Chiang, Kristian Grayson, Martin A. Green, Rose Amal, and Xunyu Lu

Sci. Adv. **11** (9), eads0836. DOI: 10.1126/sciadv.ads0836